Low-resolution transit spectroscopy of three hot Jupiters using the 2 m Himalayan Chandra Telescope

Athira Unni [1,2]★ Thirupathi Sivarani,[1] Jayesh Goyal,[3] Yogesh C. Joshi [4] Apurva V. Oza [5] and Ravinder K. Banyal[1]

[1]*Indian Institute of Astrophysics, Koramangala 2nd Block,Bangalore, 560034, India*
[2]*Department of Physics and Astronomy, University of California, Irvine, 92697, USA*
[3]*National Institute of Science Education and Research, Bhubaneswar, 752050, Odisha, India*
[4]*Aryabhatta Research Institute of Observational Sciences, Nainital, 263001, Uttarakhand, India*
[5]*Jet Propulsion Laboratory, California Institute of Technology, Pasadena, 91011, USA*

ABSTRACT

Here, we present the low-resolution transmission spectroscopy of three giant planets using the Himalayan Faint Object Spectrograph Camera (HFOSC) on the 2 m Himalayan Chandra Telescope (HCT) in Hanle, India. It is the first application of transmission spectroscopy with HCT. This study presents results from a single transit, each for three planets: HAT-P-1b, KELT-18b, and WASP-127b. The selection of suitable reference stars assisted in accurately tracking slit losses for the long cadence observations that are needed to achieve the required signal-to-noise ratio (SNR). We employ the common mode correction technique, utilizing a white light transit curve to minimize time-dependent systematic errors. The observed spectra for WASP-127b and HAT-P-1b agree with previous low-resolution transit spectroscopic observations using other observing facilities. We confirm the presence of Rayleigh scattering in the atmosphere of WASP-127b. In addition, we provide the first low-resolution transmission spectrum for KELT-18b. Modelling the exoplanet atmosphere with HFOSC and available IR observations from *HST* and *Spitzer* for WASP-127b and HAT-P-1b shows that HFOSC can be an alternative optical instrument to use in conjunction with IR observations to constrain the atmospheric parameters better.

Key words: instrumentation: spectrographs – methods: observational – techniques: spectroscopic – telescopes – planets and satellites: atmospheres – planets and satellites: gaseous planets.

1 INTRODUCTION

Exoplanet transit observation using low-resolution spectroscopy is achieved by taking a time-series of spectrophotometric observations during transit and measuring the transit depth as a function of wavelength. The observed variation of transit depth with wavelength is due to various sources of opacities set by the absorption and scattering properties of gases and aerosols near the planet's terminator (Seager & Sasselov 2000; Brown 2001). Early progress in understanding the exoplanet atmosphere started with low-resolution transit spectroscopic observations from space-based telescopes, free from Earth's telluric features (Charbonneau et al. 2002 ; Bean, Miller-Ricci Kempton & Homeier 2010; Snellen et al. 2010; Sing et al. 2016). These observations have constrained the atmospheric characteristics of several exoplanets, detecting new elements and understanding the thermal structure. Sing et al. (2016) performed a comprehensive analysis by examining the transmission spectra of ten hot Jupiters using *Hubble space telescope* (*HST*) and *Spitzer* and found that the weakened spectral signatures in the observed spectra are due to the presence of clouds and hazes present in the

atmosphere rather than the depletion of primordial water. This work also emphasizes the importance of population study of the exoplanet atmosphere to understand their formation and evolution processes.

Ground-based multi-object and long-slit observations enabled accurate differential spectrophotometry by simultaneously observing a reference star to track variable slit loss. The transiting exoplanet survey using Gemini/GMOS (Hook et al. 2004) observed several exoplanet atmospheres and showed that a single transit observation is capable of successfully constraining the atmospheric parameters (Todorov et al. 2019; Wilson et al. 2021; Panwar et al. 2022). VLT/FORS2 (Appenzeller et al. 1998) observed the upper atmospheric hazes and the presence of alkali elements in many exoplanetary atmospheres (Lendl et al. 2016; Nikolov et al. 2016; Spyratos et al. 2021), including the super-Earth GJ 1214b by Bean, Miller-Ricci Kempton & Homeier (2010). Through the ACCESS Survey, Magellan/IMACS Dressler et al. (2011) has observed the atmosphere of several planets, ranging from sub-Neptunes to inflated hot Jupiters, providing insights into their atmospheric structure, absorbers, and stellar activity (Bean et al. 2011; Rackham et al. 2017; Weaver et al. 2019). Along with characterizing diverse exoplanets, GTC/OSIRIS were able to detect potassium in the atmosphere of many planets using narrow-band spectrophotometry (Sing et al. 2012; Murgas et al. 2014; Wilson et al. 2015; Murgas et al. 2019;

★ E-mail: athira.exo@gmail.com

Chen et al. 2020). Similarly, LBT/MODS (Mallonn & Strassmeier 2016; Yan et al. 2020) also effectively contributed to ground-based low-resolution transit spectroscopic observations.

Due to the larger scale height, hot Jupiters and Saturns are the preferred candidates to observe from the ground (Seager & Sasselov 1998). Strong absorption lines of alkali metals such as Na doublets (589 nm) (Charbonneau et al. 2002; Snellen et al. 2008; Nikolov et al. 2016; Sing et al. 2016; Nikolov et al. 2018), K I doublets (767 nm) (Sing et al. 2011, 2014; Nikolov et al. 2014b; Sedaghati et al. 2016; Sing et al. 2016; Chen et al. 2018), and Li (670.7 nm) Chen et al. (2018) are most commonly detected features in the atmosphere of hot Jupiters and Saturns because of the large absorption cross-section. Rayleigh scattering in the bluer wavelength is also detectable in the visible part of the spectra (Jordán et al. 2013; Sing et al. 2014; Palle et al. 2017; May et al. 2019; Murgas et al. 2019).

A non-detection of molecular and/or atomic species (Gibson et al. 2013; Sing et al. 2014; Nortmann et al. 2016; Weaver et al. 2019) are also important. High-altitude clouds or hazes in the atmosphere of a gaseous planet can suppress the observed atomic and molecular signals in the spectra. Observations from different instruments or repeated observations for the same planet over multiple transits have sometimes revealed different results and stellar disc in-homogeneity could be a possible cause (Rackham, Apai & Giampapa 2018). Some studies using 8 m-class telescopes (Todorov et al. 2019; Jiang et al. 2023) show that it can be difficult to reproduce the detection from a smaller space-based telescopes. Also, accurate telluric correction at low resolution is challenging. Hence, ground-based transit observations are often not photon noise limited but affected by systematic errors. Repeated observations of the same planet using various instruments during various epochs will help determine the robustness of the results (Palle et al. 2017; May et al. 2019; Todorov et al. 2019).

Ground-based low-resolution transit spectroscopic observations suffer from contamination of telluric lines and variable slit losses, comparable to the amplitude of variations from the planetary atmosphere. Simultaneous multi-object observation can minimize these errors. Differential photometric corrections work well when the brightness and spectral type of comparison stars are similar to that of the target stars (Nascimbeni et al. 2013). Here we present low-resolution transit spectroscopic observations of three hot Jupiters for the first time using the 2 m Himalayan Chandra Telescope (HCT). This is also the first successful transmission spectroscopic observation ever made from HCT. The first object, HAT-P-1A is a visual binary star with a twin companion. The planet host in the system, HAT-P-1A is a G-type star with an inflated Jupiter-sized planet of radius $1.2 R_J$, mass of $0.52 M_J$, and an equilibrium temperature of 1322 K (Nikolov et al. 2014a; Bonomo et al. 2017). Nikolov et al. (2014a) detected sodium (589 nm) in the atmosphere of HAT-P-1b using HST/STIS for the first time. Subsequently, Wilson et al. (2015) successfully identified potassium using GTC/OSIRIS. Building upon this, Chen et al. (2022) detected sodium and potassium in the atmosphere of HAT-P-1b using P200/DBSP telescope. However, the 8 m Gemini/GMOS (Todorov et al. 2019) observation could not confirm sodium detection. Furthermore, Montalto et al. (2015) observed only a blue edge of the sodium broad absorption wing using DOLORES/TNG observations.

The second object, WASP-127, is the puffiest, low-density planet around a G5 star, also part of a binary system, and hosts a planet with an equilibrium temperature of 1400 K, radius of $1.37 R_J$ and mass of $0.18 M_J$ in the transition region of Jupiter to Neptune mass (Lam et al. 2017). *HST* and *Spitzer* observations by Skaf et al. (2020) and Spake et al. (2021) showed feature-rich transit spectra with absorption

from sodium and wavelength-dependent Rayleigh scattering in the optical. Palle et al. (2017) studied the atmosphere of WASP-127b using 2.5 m NOT/ALFOSC and detected a strong Rayleigh scattering slope and a hint of sodium detection. The third target, KELT-18 is a single star hosting a massive planet of $R_p = 1.57 R_J$ and $M_p = 1.18 M_J$ (McLeod et al. 2017), and this work presents low-resolution transit spectroscopy for KELT-18b for the first time. In the case of HAT-P-1A and WASP-127, we used the binary companion star as the reference star, and for KELT-18, we used the nearby bright field star as a reference star. None of the three reference stars are known to be variable. Our attempt of demonstrating the feasibility of a 2 m class telescope will encourage the community to use more similar telescopes for observing the exoplanet atmosphere.

The paper is organized as follows. Section 2 covers the observations, while Section 3 explains the data reduction and analysis. Section 4 presents details of the modelling of the observed data and the results obtained. Finally, the discussion and conclusions are presented in Section 5. Additional figures supporting this study can be found in Appendix A.

2 OBSERVATIONS

Observations are obtained from the Indian Astronomical Observatory (IAO) at Hanle, the Ladakh region of the Himalayas, operated by the Indian Institute of Astrophysics. We use Himalayan Faint Object Spectrograph Camera (HFOSC),[1] a low-resolution slit spectrograph uses different grisms and slits of varying widths and lengths, mounted on the 2 m HCT. HFOSC has a field of view of 10 arcmin × 10 arcmin and a 2048 × 4096 SITe detector with a pixel scale of 0.296 arcsec. We used grism-8 and grism-7 to cover the wavelength range of 3800 to 6500 Å and 5800 to 8350 Å, respectively. We performed differential spectrophotometry with the longest and widest available slit (11 arcmin × 15.41 arcsec) to minimize the time variable slit loss and maximize field of view (FOV) with a resolution of 1180 (grism-7, at 5900 Å) and 1920 (grism-8, at 7800 Å). Only one of the grism settings is used for a given transit; hence, the entire optical wavelength range is not covered simultaneously. Choosing a reference star is also essential to minimize differential slit loss between the target and reference as a result of atmospheric dispersion, seeing, and other environmental and instrument effects. A good reference star could be a visual twin binary companion or a field star of similar spectral type and brightness to the target star. Due to the FOV, we are also limited to a maximum separation of 11 arcmin between the exoplanet host and a reference star. During observation, we aligned the slit along the target star and the reference star by changing the position angle of the instrument cube in the cassegrain unit so that simultaneous observations of the target and reference are possible. The details of the observations and objects are given in Table 1 and Table 2, respectively.

3 DATA REDUCTION

Initial data reduction was carried out using IRAF (image reduction and analysis facility), which includes bias correction, flat fielding, and optimal aperture extraction. The dispersion solution for the wavelength calibration is derived from the arc lamps (FeAr and FeNe for Grism 7 and Grism 8, respectively). The calibration lamp exposures were taken during the beginning and end of the transit

---

[1] https://www.iiap.res.in/?q = iao_2m_hfosc

Table 1. Observational details: Name of the target, date of observation (DoO), peak signal-to-noise ratio per exposure (SNR), exposure time (Exp.time), number of exposures (No.Exp), parallactic angle (PA) in degrees, position angle (PoA) in degrees, airmass at the beginning and end of the observation, grism used, and the corresponding wavelength coverage, and the name of the reference star used are listed.

Object	DoO	SNR	Exp.time	No.Exp	PA	PoA (E of N)	Airmass	Grism	Wavelength range	Reference star
WASP-127	$09 - 03 - 2019$	909	420s	62	339.19	78.2	1.99–1.99	7	3800–6500 Å	TYC 4916-897-1
HAT-P−1A	$02 - 07 - 2018$	944	180s	57	272.45	−99.5	1.55–1.02	7	3800–6500 Å	HAT-P−1B
KELT-18	$10 - 06 - 2019$	1075	420s	55	125.34	2.0	1.15–1.74	8	5800–8350 Å	TYC 3865-1339-1

Table 2. Stellar parameters: Name of the target star and the reference star (Object), visual magnitude (Vmag), effective temperature (T_{eff}) in Kelvin, the logarithm of gravity ($\log g$), and metallicity ([Fe/H]) and separation between the target and the reference star are given below.

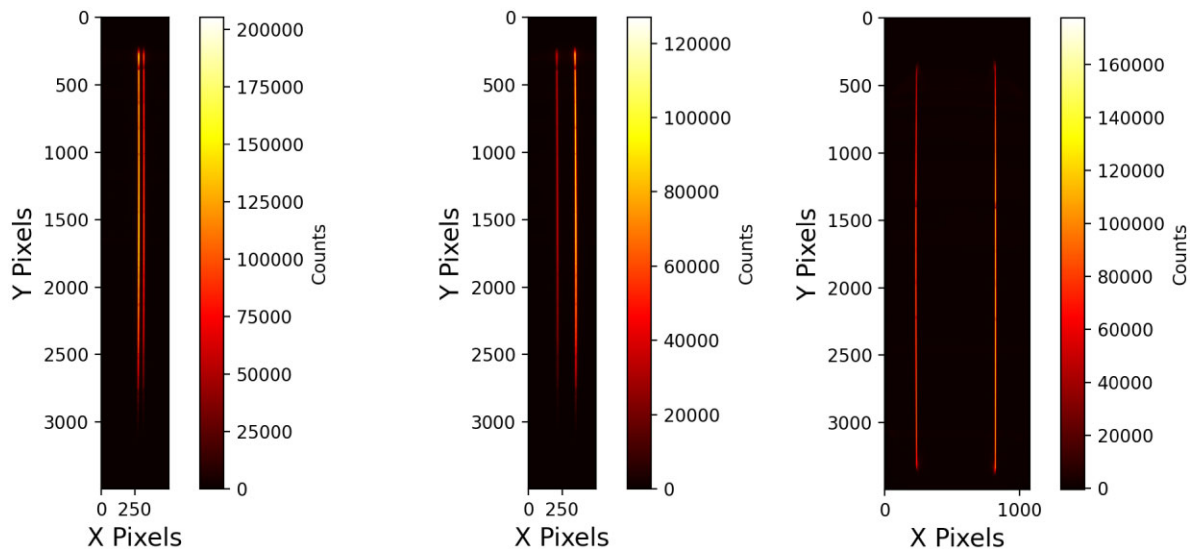| Object	Vmag	T_{eff}	$\log g$	[Fe/H]	Separation
WASP-127	10.20	5750 ± 100	3.90 ± 0.1	-0.18 ± 0.06	41.8 arcsec
TYC 4916-897-1	11.0	5733	4.480	...	...
HAT-P−1A	10.4	6047 ± 56	4.13 ± 0.10	0.12 ± 0.05	11.2 arcsec
HAT-P−1B	9.87	5975 ± 45	4.45 ± 0.06	0.13 ± 0.02	...
KELT-18	10.4	6670 ± 120	4.034 ± 0.083	0.08 ± 0.13	5.79 arcmin
TYC 3865-1339-1	9.92	6787	3.976	...	...

Figure 1. HCT/HFOSC single exposure CCD images of HAT-P-1A, WASP-127, and KELT-18, along with the reference star from left to right. The horizontal and vertical axis correspond to the position along the slit and the wavelength, respectively.

observations with the same setup as the science exposures, but using a narrower slit of width 1.92 arcsec. Fig. 1 shows the 2D image of the spectra for all three objects. Since the on-sky observations were taken continuously (without calibration lamp exposures) for several hours, a wavelength drift of the spectra is expected due to instrument flexure, temperature changes, and seeing. Any shifts between the first exposure (that is, taken closer to the lamp spectrum) and subsequent exposures are corrected by finding the offset and applied to the dispersion solution. We used the centroid shift in the prominent telluric lines in each exposure to estimate the offset. Visually inspecting the individual spectra by overplotting with the first exposure seems to be well aligned within a pixel accuracy. The wavelength shift from first to last exposure for the three targets is less than 4 pixels or 3 Å. The wavelength offset between the reference and target star spectra on the detector was also adjusted for each exposure. The typical offset is 1.2, 2.15, and 6.5 Å for WASP-127, HAT-P-1A, and KELT-18, respectively. Fig. 2 represents the

wavelength-calibrated spectra of the target star and reference from the same exposure.

3.1 Constructing the white light curve

A transit white light curve was constructed by integrating the flux over the observed wavelength range of both the target and the reference star in each exposure. Individual white light curve of the target and the reference star are shown in Fig. 3. A differential white light curve is constructed by dividing the target star light curve by the reference star light curve. This technique assumes that the time-dependent systematic errors are the same in the observed flux of both the target and reference stars. We removed all the telluric regions when constructing the white light curve to avoid introducing additional systematic errors.
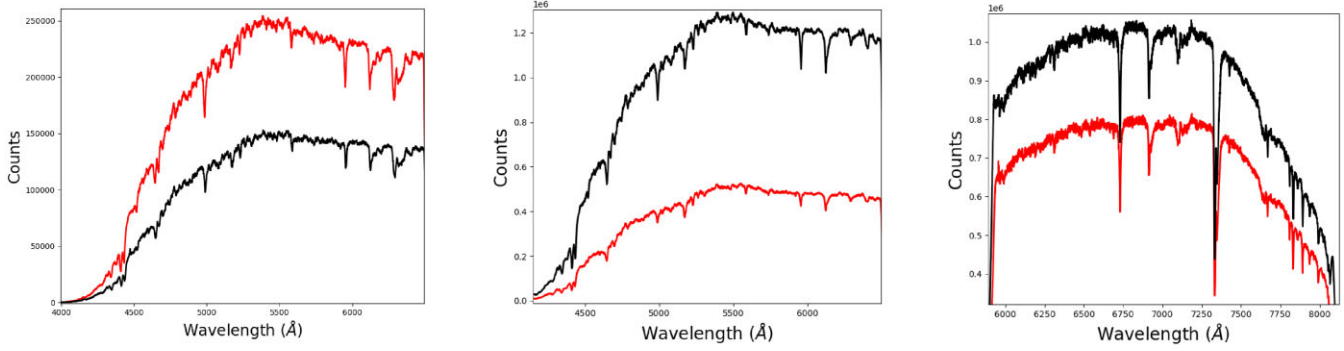
Figure 2. Single exposure, wavelength calibrated spectra of HAT-P-1A (Grism 7), WASP-127 (Grism 7), and KELT-18 (Grism 8) from left to right. The solid black line is the object star and the solid red line is the reference star.
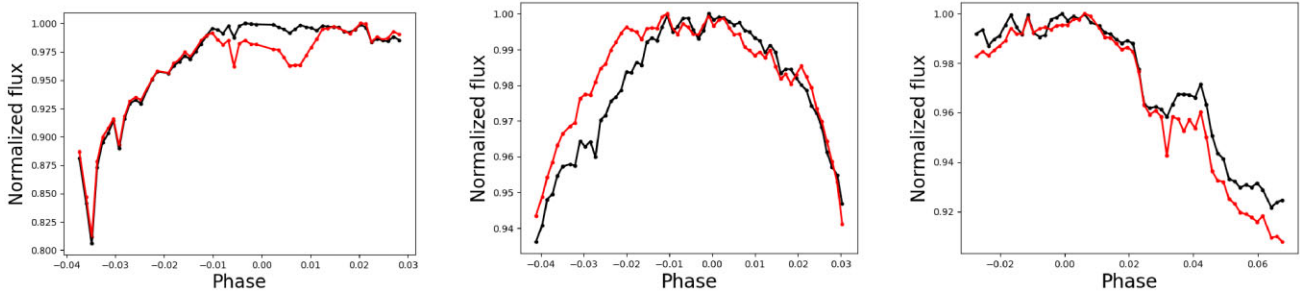

Figure 3. Individual light curves of object star (black) and the reference star (red) follows similar trend as a function of time. HAT-P-1A, WASP-127, and KELT-18 from left to right, respectively.

The best-fitting model to the light curve was obtained using PYTRANSIT[2] (Parviainen 2015), a python-based light-curve modelling tool widely used for exoplanet detection and characterization (Casasayas-Barris et al. 2022; Jiang et al. 2022).PYTRANSIT provides efficient CPU and GPU implementations and combines a Bayesian approach to inference with Markov chain Monte Carlo (MCMC) (Foreman-Mackey et al. 2013) sampling for the posterior estimation. This package includes various transit models like Mandel & Agol (2002), Giménez (2006), Maxted & Gill (2019), and Parviainen (2020) with various limb darkening laws. Out of this, we used the popular Mandel-Agol analytic transit light-curve model with quadratic limb darkening law. The primary input to PYTRANSIT are the normalized, detrended flux in the user-defined wavelength region and the observation time of each exposure. A second-order polynomial function is used for detrending the light curve in time. The mid-transit time (T_c) and the transit depth from previous studies were used as prior parameters for the subsequent MCMC run (30 chains of 2000 iterations) to obtain a reasonable posterior distribution of the parameters using the Bayesian approach. The adopted mid-transit time for HAT-P-1b, WASP-127b, and KELT-18b are 2453979.932 (Nikolov et al. 2014a), 2458293.252 (Spake et al. 2021), and 2457542.525 (McLeod et al. 2017), respectively. We used a transit depth of 0.01392 (Nikolov et al. 2014a), 0.01013 Spake et al. (2021), and 0.00716 (McLeod et al. 2017) for HAT-P-1b, WASP-127b, and KELT-18b, respectively. These initial values are optimized with other parameters like the orbital inclination, impact parameter, and stellar density. The orbital period of all three targets are fixed in the analysis. We used an orbital period of 4.46529976 d (Nikolov et al. 2014a), 4.17807015 d (Skaf et al. 2020), and 2.8717510 d

(McLeod et al. 2017) for HAT-P-1b, WASP-127b, and KELT-18b, respectively. The orbital eccentricity of all three targets was fixed at zero, assuming a circular orbit. The quadratic limb-darkening coefficients are estimated for each target using PYTRANSIT and fixed for a model. Along with the fixed parameters, Table 3 shows all the transit parameters obtained from the best-fitting white light curves for all three targets. For example, the posterior density distribution of different parameters for HAT-P-1b is shown in Fig. A1 in the Appendix.

3.2 Constructing low-resolution transmission spectra

We applied the common mode correction (CMC) technique (Gibson et al. 2013; Stevenson et al. 2014; Weaver et al. 2019; Wilson et al. 2020) to remove dominant time-dependent systematics (common across all wavelengths) from the individual spectroscopic light curves. This entailed dividing the data into wavelength bins such that the SNR of individual spectroscopic light curves was always 1000. Then, we calculated the residuals from the white light-curve fits (discussed in Section 3.1) – that is, the observed white light curve divided by the best-fitting model. This is the 'common mode' noise. We divided each of the spectroscopic light curves by the common mode noise to construct the common mode corrected light curves. By employing CMC, we sacrifice the information of the absolute transit depths and instead obtain relative transit depths, but this approach will avoid most of the time-dependent scatter in the light curves and improve the precision of the measured transit depths in all wavelength channels. We fit the individual wavelength-dependent light curves using PYTRANSIT following the similar procedure explained in Section 3.1 with the parameters from the best-fitting white light curve as prior input. Figs 4, 5, and 6

[2]https://github.com/hpparvi/PyTransit

Table 3. The best-fitting parameters from white light curve using the posterior density distribution. The orbital period (*P*) in days, the mid-transit time T_c in JD, orbital inclination (i) in degrees, impact parameter (b), quadratic limb darkening coefficients u and v, orbital eccentricity (e), and the planet to star radius ratio (R_p/R_*) are listed below.

Parameters	HAT-P−1b	WASP-127b	KELT-18b	
P (d)	4.4652	4.1780	2.8716	fixed
T_c	2459079.3110±0.0003	2458552.3070 ± 0.0321	2458645.2389 ± 0.0014	fitted
i (deg)	85.37 ± 0.8594	89.38 ± 0.3036	89.15 ± 1.7188	fitted
b	9.85 ± 0.2391	7.89 ±0.0101	5.14 ± 0.0101	fitted
u	0.3005	0.6550	0.2704	fixed
v	0.4913	0.5399	0.3904	fixed
e	0	0	0	fixed
R_p/R_*	0.1122 ± 0.0015	0.0964 ± 0.0016	0.0902 ± 0.0017	fitted
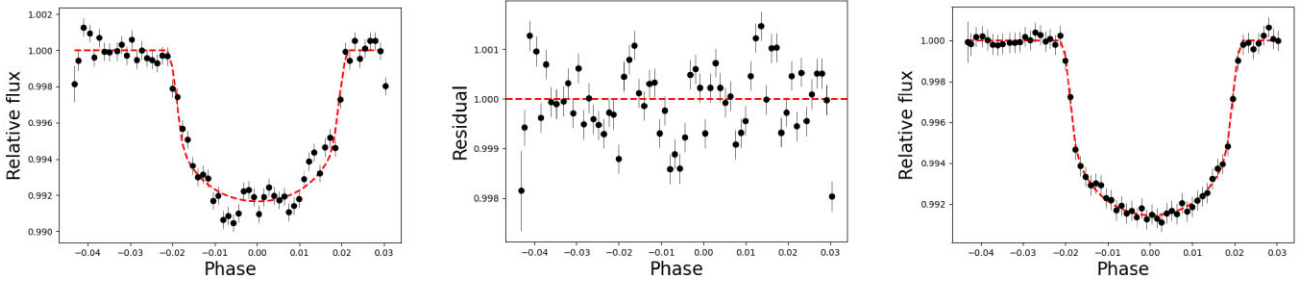
Figure 4. Observed white light curve (scattered point) of WASP-127 with the best-fitting model (dashed line) in left after detrending in time. The residual plot in the centre and the light curve after applying the common mode correction is on the right.
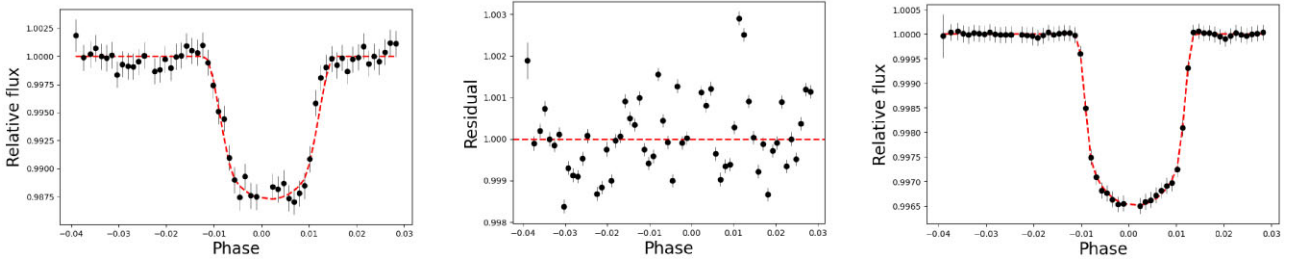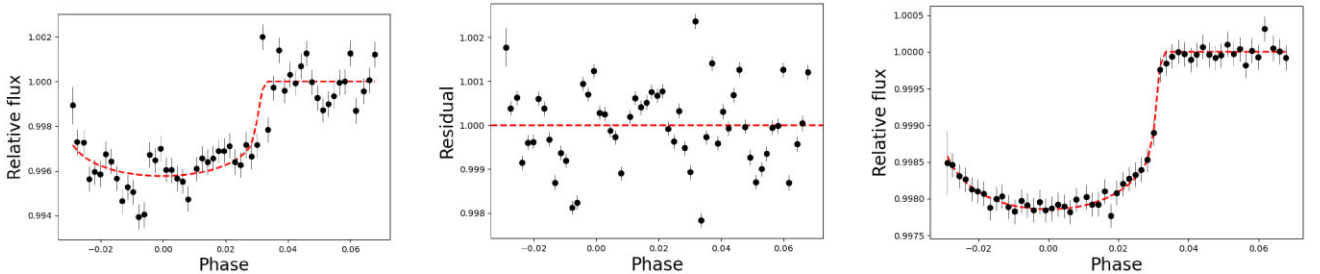

Figure 5. Observed white light curve (scattered points) of HAT-P-1b with the best-fitting model (dashed line) in left after detrending in time. The residual plot in the centre and the light curve after applying the common mode correction is on the right.

Figure 6. Observed white light curve (scattered points) of KELT-18 with the best-fitting model (dashed line) in left after detrending in time. The residual plot in the centre and the light curve after applying the common mode correction is on the right. The ingress part of the transit is missed due to instrument failure during the observation.

demonstrate the method for constructing the common mode corrected spectroscopic light curves for WASP-127b, HAT-P-1b, and KELT-18b, respectively (a typical single wavelength bin of SNR = 1000 is shown for each).

Chromatic dispersion and achromatic differential refraction are the two different components that contribute to slit loss during the observation. As the chromatic dispersion is constant for a field, a differential analysis can minimize the effects even though the ideal situation is to have an atmospheric dispersion corrector (ADC). All three objects and the corresponding reference stars have similar physical parameters (see Table 2), so it is unlikely that the differential atmospheric dispersion will contribute to these observations. The
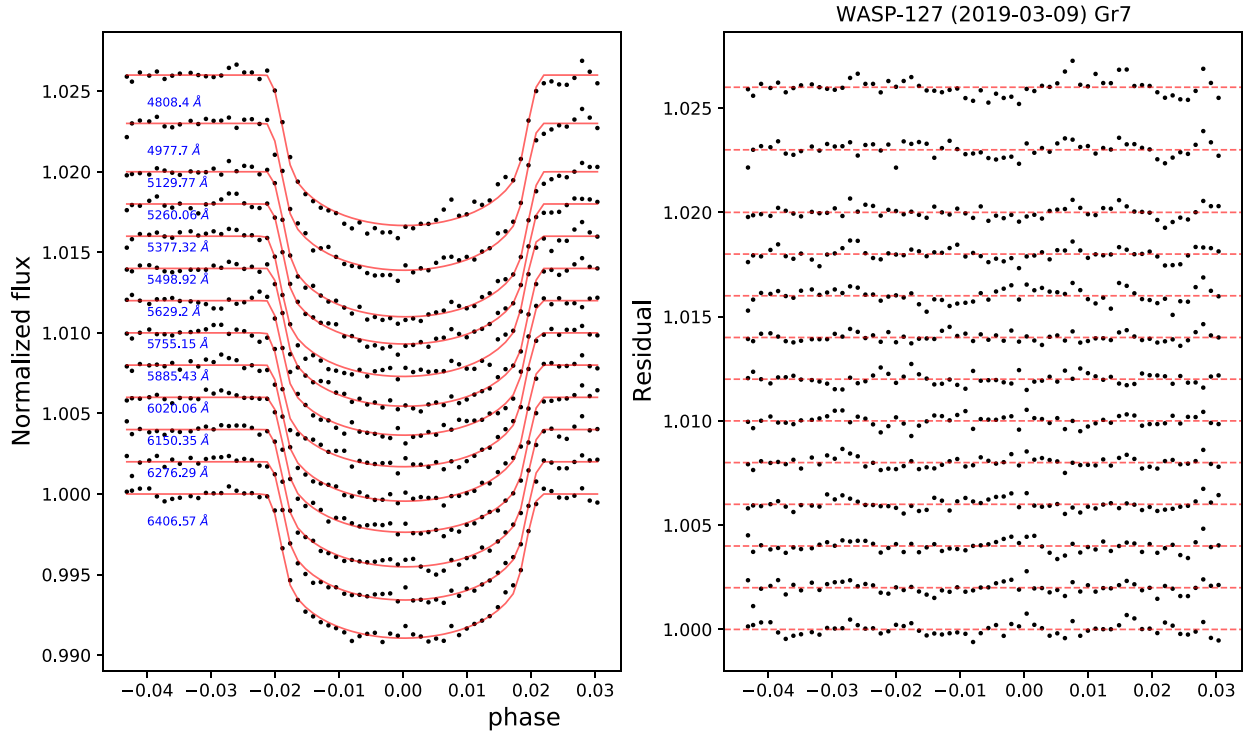
Figure 7. Grism 7 light curves in each wavelength bin (scattered points) and the best-fitting transit models (solid lines) stacked from top to bottom for WASP-127b. A constant offset of 0.01 is added to the light curves in y-direction for clear separation. A wavelength bin of constant SNR = 1000 is used for constructing the light curves.

field differential refraction is due to the airmass variation in the FOV. We estimated the apparent shift in the position of the stars due to differential refraction using equation (3) in Sánchez-Janssen et al. (2014) for the airmass ranges in our study (Table 1) and considering the binary separation (Table 2). It is 0.005 arcsec − 0.002 arcsec for HAT-P-1A, 0.03 arcsec − 0.03 arcsec for WASP-127, and 0.09 arcsec − 0.2 arcsec for KELT-18 at the beginning and end of the observation. The values are smaller than the slit width (15.4 arcsec), so differential refraction is unlikely to play a significant role in these observations. Any significant variations as a function of time would be due to the instrumental effects, which can be removed using CMC. The common mode corrected light curve at different wavelength bins for all three targets presented in Figs 7, 8, and 9. The transit depth measured at different wavelength bins is presented in Tables 4, 5, and 6 for KELT-18b, HAT-P-1b, and WASP-127b, respectively.

4 MODELLING THE TRANSMISSION SPECTRA

To interpret the observed transmission spectra of HAT-P-1b and WASP-127b, we used a grid of chemical-equilibrium model atmospheres and their calculated transmission spectra, which were developed using ATMO (Goyal et al. 2017). ATMO is a 1D planetary atmosphere model that can compute radiative–convective equilibrium pressure–temperature ($P–T$) profiles consistent with equilibrium as well as dis-equilibrium chemistry (Amundsen et al. 2014; Tremblin et al. 2015; Drummond et al. 2016; Goyal et al. 2017, 2020). The transmission spectra model grid used in this work assumes an isothermal $P–T$ profile and equilibrium chemistry with condensation as described in detail in Goyal et al. (2017). The grid consists of a total of 3920 model transmission spectra for each

planet for a range of isothermal temperatures (T_{eq} − 300 to T_{eq} + 300), metallicity (0.005–200× solar), C/O ratio (0.15–1.5). Haze is parametrized using a multiplicative haze factor ranging from 1 to 1100 times the Rayleigh scattering opacity due to gases in the atmosphere. Clouds are treated as large particles and parametrized with an additive grey opacity ranging from 0 (no cloud) to 1 times the H_2 Rayleigh scattering cross-section at 350 nm. A detailed explanation of the model and grid parameters is provided in Goyal et al. (2017). The spectral resolution of the model used for this analysis is $R = 5000$ at 0.2 μm while decreasing to $R = 100$ at 10 μm. The best-fitting models are determined by χ^2 minimization by re-binning the model spectra to the observed data. This model grid has been extensively used to interpret several ground-based observations (e.g. Carter et al. 2020; Wilson et al. 2020; Spyratos et al. 2021; Weaver et al. 2021). The Figs 10 and 11 show the observed transmission spectra with the corresponding best-fitting model spectra for HAT-P-1b and WASP-127b, respectively.

For HAT-P-1b, we find that the best-fitting model has a temperature of 1622 K, 0.005× solar metallicity, C/O ratio of 1.5, Haze-factor of 1100, and cloud-factor of 0. The best-fitting model has χ^2 = 6.67 with $0.75 \leq P(\chi^2) \leq 0.9$. We could not find evidence of any molecular/atomic species with the current data set. We show the 3σ range of the model parameters with respect to the best-fitting model with a χ^2 map for HAT-P-1b in Fig. 12. The methodology for plotting this χ^2 map is the same as discussed in Goyal et al. (2017). From these plots, we can infer that we are not able to constrain metallicity, C/O ratio, and clouds robustly for HAT-P-1b with the HFOSC observations. The only physical characteristic that we were able to constrain to some extent is the Rayleigh scattering slope, with the presence of enhanced Rayleigh scattering haze, which for the best-fitting model is 1100 times the nominal Rayleigh scattering,
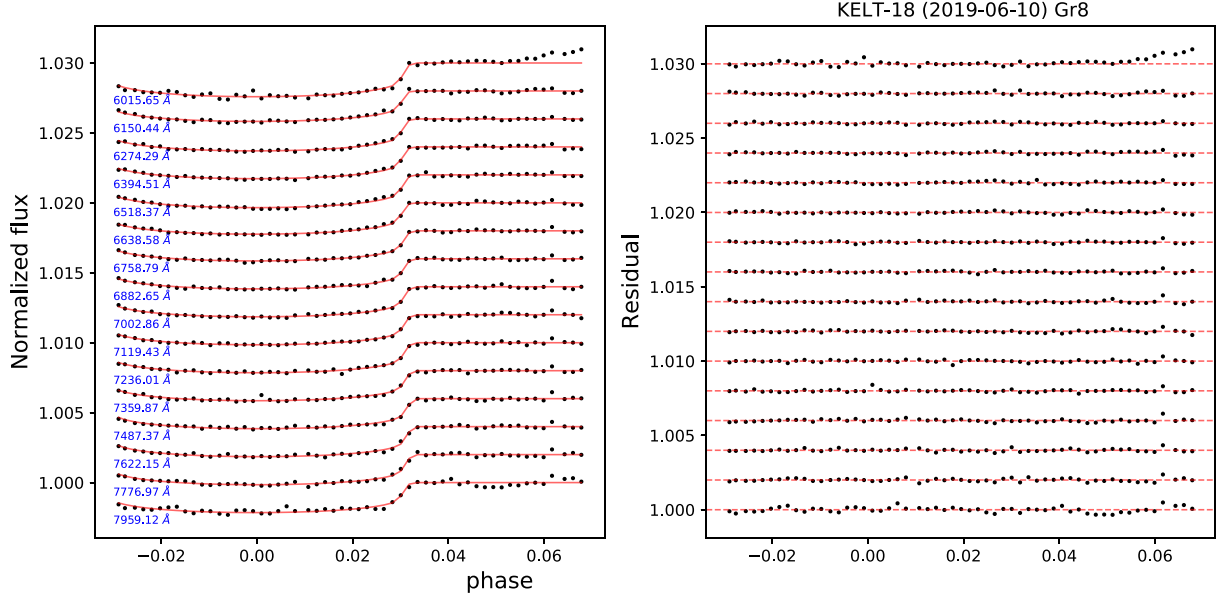
Figure 8. Grism 8 light curves in each wavelength bin (scattered points) and the best-fitting transit models (solid lines) stacked from top to bottom for KELT-18b. A constant offset of 0.01 is added to the light curves in y-direction for clear separation. A wavelength bin of constant SNR = 1000 for constructing the light curves.
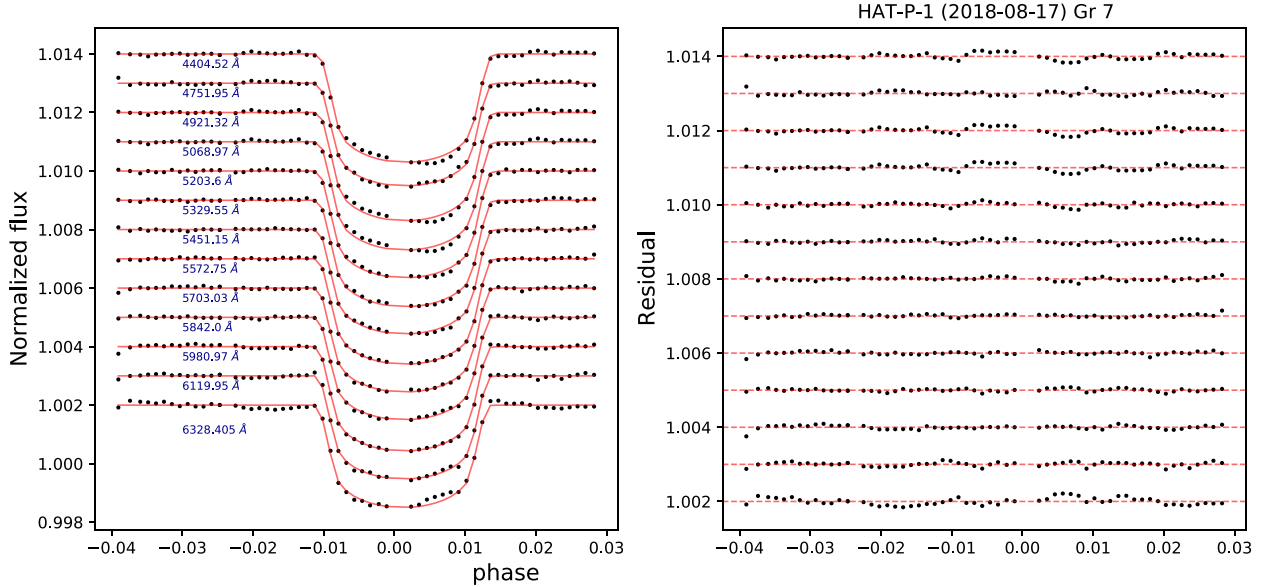

Figure 9. Grism 7 light curves in each wavelength bin (scattered points) and the best-fitting transit models (solid lines) stacked from top to bottom for HAT-P-1b. A constant offset of 0.01 is added to the light curves in y-direction for clear separation. A wavelength bin of constant SNR = 1000 is used for constructing the light curves.

with values between $10\times$ to $1100\times$ (logarithmically spaced) within the 1σ range of the minimum χ^2 model.

For WASP-127b, we find that the best-fitting model has a temperature of 1700 K, $0.005\times$ solar metallicity, C/O ratio of 0.35, Haze-factor of 150, and cloud-factor of 1. The best-fitting model has $\chi^2 = 5.71$ with $0.95 \leq P(\chi^2) \leq 0.99$. For WASP-127b, too, we are only able to constrain the Rayleigh scattering slope, with the presence of enhanced Rayleigh scattering haze. The haze factor for the best-fitting model is 150 times the nominal Rayleigh scattering, with values between $10\times$ to $1100\times$ within the 3σ range of the minimum

χ^2 model. However, as metallicity increases, the haze factor is strongly constrained to values larger than $150\times$. For metallicities greater than $100\times$ solar, the haze factor lies between $150\times$ and $1100\times$, that too within the 3σ range of the minimum χ^2 model as shown in the χ^2 map for WASP-127b (Fig. 13). The large value of the haze factor implies a substantially hazy atmosphere, which is consistent with interpretation using GTC observations from Chen et al. (2018) but inconsistent with *HST* observations from Spake et al. (2021). However, we do not detect the presence of Na as in Chen et al. (2018) and Spake et al. (2021) due to the lower precision

Table 4. Observed transit depth of constant SNR = 1000 for KELT-18b. The central wavelength (W) in Å, width of each wavelength bin (Å), the planet to star radius ratio (R_p/R_*), and error in the estimate R_p/R_* are presented in columns one to four, respectively.

W (centre)	W (width)	R_p/R_*	R_p/R_*(err)
7959.12	100.18	0.07347	0.00255
7776.97	81.96	0.07343	0.00242
7622.15	72.85	0.07452	0.00229
7487.37	61.93	0.07211	0.00126
7359.87	61.93	0.07215	0.00188
7236.01	58.29	0.07146	0.00148
7119.43	58.43	0.07229	0.00162
7002.86	58.28	0.07179	0.00158
6882.65	61.93	0.07164	0.00121
6758.79	61.92	0.07158	0.00115
6638.58	58.28	0.07252	0.00110
6518.37	61.93	0.07396	0.00120
6394.51	61.93	0.07343	0.00115
6274.29	58.28	0.07325	0.00102
6150.44	66.37	0.07142	0.00098

Table 5. Observed transit depth of constant SNR = 1000 for HAT-P−1b. The central wavelength (W) in Å, width of each wavelength bin (Å), the planet to star radius ratio R_p/R_*, and error in the estimate (R_p/R_*) are presented in columns one to four, respectively.

W (centre)	W (width)	R_p/R_*	R_p/R_*(err)
6328.405	138.8	0.11998	0.00197
6119.95	69.4	0.11961	0.00198
5980.97	69.4	0.12031	0.00188
5842.0	69.4	0.11932	0.00191
5703.03	69.4	0.12008	0.00186
5572.75	60.8	0.12119	0.00202
5451.15	60.8	0.12118	0.00199
5329.55	60.8	0.12212	0.00208
5203.6	65.1	0.12295	0.00218
5068.97	69.4	0.12410	0.00224
4921.32	78.1	0.12079	0.00220
4751.95	91.2	0.12563	0.00223
4404.52	256.2	0.12134	0.00296

Table 6. Observed transit depth of constant SNR = 1000 for WASP-127b. The central wavelength (W) in Å, width of each wavelength bin (Å), the planet to star radius ratio (R_p/R_*), and error in the estimate (R_p/R_*) are presented in columns one to four, respectively.

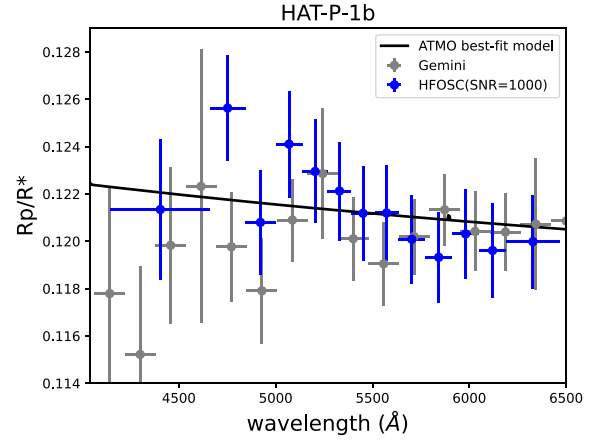| W (centre)	W (width)	R_p/R_*	R_p/R_*(err)
6406.57	69.48	0.09747	0.00117
6276.29	60.8	0.09702	0.00136
6150.35	65.14	0.09676	0.00115
6020.06	65.14	0.09618	0.00140
5885.43	69.48	0.09661	0.00133
5755.15	60.8	0.09619	0.00083
5629.2	65.1	0.09615	0.00185
5498.92	65.1	0.09681	0.00117
5377.32	56.4	0.09758	0.00138
5260.06	60.8	0.09728	0.00167
5129.77	69.4	0.09838	0.00160
4977.7	82.5	0.09892	0.00243
4808.4	86.8	0.09955	0.00210

Figure 10. The best-fitting ATMO model with HCT/HFOSC transmission spectra observations of HAT-P-1b, overplotted with earlier observations from 8.1 m Gemini/GMOS (Todorov et al. 2019).
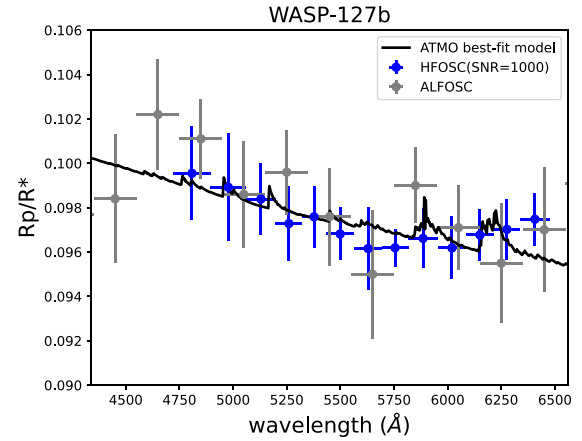

Figure 11. The best-fitting ATMO model with HCT/HFOSC transmission spectra observations of WASP-127b, overplotted with earlier observations from 2.5 m NOT/ALFOSC (Palle et al. 2017).
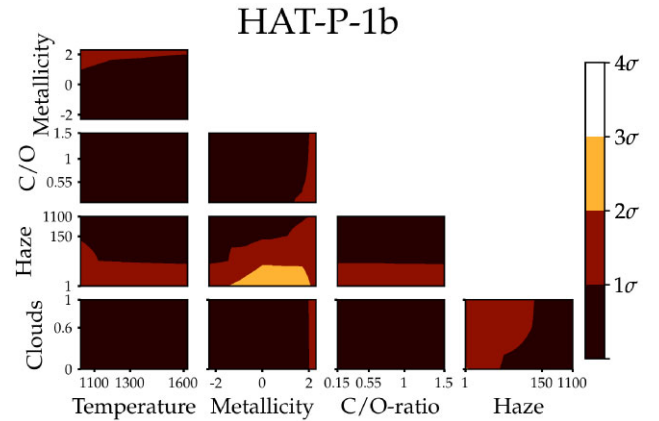

Figure 12. The χ^2 map for HAT-P-1b. Contours of χ^2 are shown for all the combinations of grid parameters. Cloud and haze factor axes are log-scaled. Metallicity is also log-scaled, 0 being solar metallicity and 2 being 100 times solar metallicity. The colours indicate confidence intervals as shown in colourmap to the right.
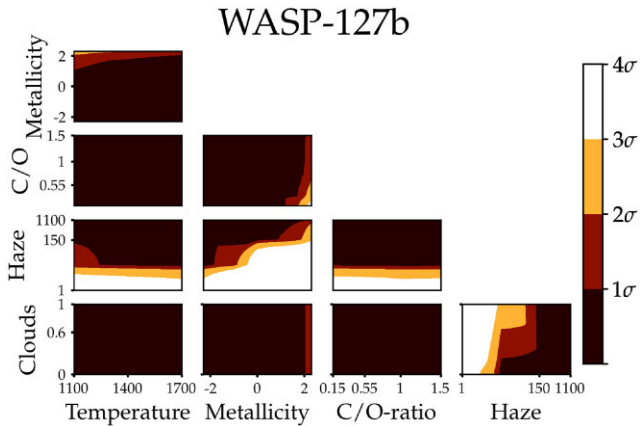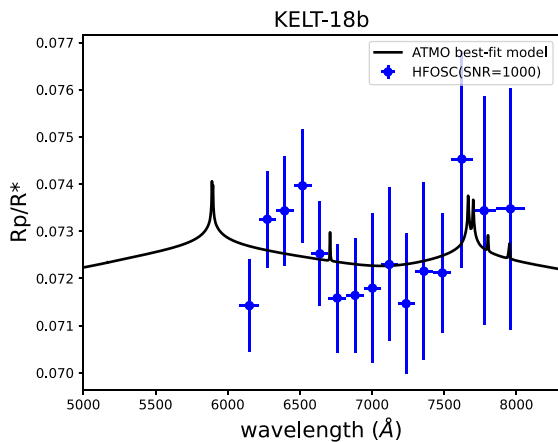
WASP-127b

Figure 13. The χ^2 map for WASP-127b. Contours of χ^2 are shown for all the combinations of grid parameters. Cloud and haze factor axes are log-scaled. Metallicity is also log-scaled, 0 being solar metallicity and 2 being 100 times solar metallicity. The colours indicate confidence intervals as shown in colourmap to the right.

KELT-18b

Figure 14. The Best-fitting ATMO model with HCT/HFOSC transmission spectra observations of KELT-18b.

and spectral resolution of the HFOSC data. The best-fitting model predicts TiO/VO spectral features similar to Palle et al. (2017), but the precision and wavelength coverage of the current data set do not allow us to constrain it in any way.

Since for KELT-18b, the model transmission spectra were not available in the planet-specific library presented in Goyal et al. (2017), we, therefore, used ATMO generic grid scalable model spectra as presented in Goyal et al. (2018). This model grid can be used to scale to any planet's transmission spectra with H_2-He dominated atmosphere across a range of temperatures (400–2600 K), planetary gravities (5–50 m s^{-2}), atmospheric metallicities (1×–200× solar), C/O ratio (0.35–1), haze-factor (1–1100), and cloud-factor (0–1). This model grid also assumes isothermal P–T profiles. For KELT-18b, the best-fitting model has a temperature of 1200 K, 10× solar metallicity, C/O ratio of 1 without any haze and clouds. The best-fitting model has $\chi^2 = 6.32$ with $0.90 \leq P(\chi^2) \leq 0.95$. Due to the extremely low precision of this KELT-18b data, we are not able to constrain any physical or chemical characteristics with our models. The best-fitting ATMO model, along with the observed HFOSC data for KELT-18b, is shown in Fig. 14.

To demonstrate the advantage of HFOSC observations and place more robust constraints on the estimated parameters for both HAT-P-1b and WASP-127b, we fitted the model grid with the HFOSC observations along with available high quality *HST/Spitzer* observations in the infrared. Fig. A2 in Appendix shows the best-fitting model from the HAT-P-1b model grid, when fitted to HFOSC observations combined with *HST* observations from Wakeford et al. (2013). The offset between HFOSC and *HST* is a free parameter when fitting models to observations. The best-fitting model gives an equilibrium temperature of 1472 K, solar metallicity, C/O ratio of 0.15 (subsolar), Haze-factor of 1100, and cloud-factor of 0 (no clouds). The best-fitting model has a χ^2 value of 32.57 with 39 degrees of freedom. The best-fitting offset value between HFOSC and *HST* observations is -0.0029. Fig. A3 and A4 in the Appendix show the χ^2 maps for HAT-P-1b model grid when fitted to just *HST* infrared observations and HFOSC plus *HST* observations, respectively. It can be clearly seen from the χ^2 maps that the 3σ constraints on the model parameters are better with HFOSC plus *HST* infrared observations as compared to just *HST* infrared observations and HFOSC observation. Specifically, we are able to put robust constraints on the haze parameter, as expected, since we can constrain the Rayleigh scattering slope of the transmission spectrum with HFOSC observations. The combined spectrum constrains the C/O ratio to be less than 0.7 and the metallicity to be within 0.1× and 50× solar metallicity. It also helps place stronger constraints on the equilibrium temperature of the planet, with preference towards higher equilibrium temperature, as seen in the χ^2 maps. While *HST* infrared observations help in placing stronger constraints on the C/O ratio and metallicity, HFOSC observations help in placing stronger constraints on the haze parameter and temperature.

Fig. A5 in the Appendix shows the best-fitting model from the WASP-127b model grid when fitted to HFOSC observations combined with infrared observations from *HST* and *Spitzer* (Spake et al. 2021). We find that the best-fitting model has a temperature of 1100 K, 10× solar metallicity, solar C/O ratio, Haze-factor of 150, and a cloud-factor of 1.0. The best-fitting model has a χ^2 value of 57.16 with 42 degrees of freedom. The best-fitting offset value between HFOSC and *HST/Spitzer* observations is 0.0048. Figs A6 and A7 in the Appendix show the χ^2 maps for WASP-127b model grid when fitted to just infrared *HST/Spitzer* observations and HFOSC plus *HST/Spitzer* observations, respectively. It can be clearly seen from the χ^2 maps that the 3σ constraints on the model parameters are better with HFOSC plus *HST/Spitzer* observations as compared to just *HST/Spitzer* observations in the infrared. Similar to HAT-P-1b, the constraints are worse with just HFSOC observations, significantly better with just *HST/Spitzer* observations and best with the combined observed spectra. With just HFOSC observations we are able to constrain the haze parameter to be greater than 10× the multigas Rayleigh scattering while all the other model parameters are unconstrained. However, with just *HST/Spitzer* observations we obtain very strong 3σ constraints on the equilibrium temperature ($T_{eq} \leq$ 1250), metallicity ($1 \leq Z \leq 1.7$), C/O ratio ($0.35 \leq C/O \leq 0.56$), and haze-factor ($150 \leq$ haze-factor ≤ 1100), without any constraints on the cloudiness factor. With the addition of HFOSC observations to this *HST/Spitzer* spectrum in IR, the constraints on the equilibrium temperature become more robust ($T_{eq} \leq 1100$), the metallicity constraints remain same but the favoured metallicity (within 1σ) shifts to 10× solar, the haze factor constraints also remain same but the favoured haze-factor (within 1σ) shifts to 150× multigas Rayleigh scattering compared to 1100× with just *HST/Spitzer* observations. Additionally, with the combined observations, we are able to place constraints even on the cloud factor (cloud-factor ≥ 0.2), basically

discarding the no-cloud scenario. In summary, although we are able to place robust constraints with just *HST/Spitzer* observations in IR as compared to just HFOSC observations for WASP-127b, these constraints become more robust when both spectra are combined, especially for estimating equilibrium temperature, metallicity, haze, and clouds.

5 DISCUSSION AND CONCLUSION

In this paper, we present the low-resolution transit spectroscopic observation from HCT/HFOSC instrument for the first time. The wavelength-dependent light curves (Figs 7, 8, and 9) are relatively free from systematic errors after CMC with the RMS amplitude of residuals only 0.002 times above the expected photon noise after detrending in time. Relatively good precision is achieved mainly because of the availability of a suitable reference star for all three targets otherwise the CMC can underestimate the error in the transit depth and can misinterpret the transmission spectra (Jiang et al. 2022). The ideal reference star is a binary twin companion as in the case of HAT-P-1A and WASP-127.

We have tried different SNR (SNR = 200, SNR = 500, and SNR = 1000) bins to understand the optimal SNR to construct the transmission spectra. Although the number of data points in the spectra increases with lower SNR bins, the estimated error in the transit depth also increases. So, there should always be a balance between the number of data points required and the accuracy of the estimated transit depth needed. We explored the sodium doublet region separately for WASP-127b and HAT-P-1b, choosing a narrow bandwidth of constant SNR = 500 to detect the possible detection of sodium around 5890 Å and the possible detection of potassium around 7670 Å region for KELT-18b following the method explained in Section 3. Unfortunately, we could not detect sodium or potassium above the uncertainty level. Therefore, we recommend using wavelength bins of 70 Å or SNR = 1000 for studying systems similar to WASP-127b and HAT-P-1b with HCT/HFOSC. For example, Fig. A8 in the Appendix presents the observed spectra of WASP-127b in all three bins (SNR = 200, SNR = 500, and SNR = 1000) using HFOSC.

Even though the HCT/HFOSC observations are in decent agreement with the previous ground-based observations with the same technique, we could not detect any atomic/molecular species using the best-fitting ATMOmodels for all three targets. In the case of WASP-127b, the equilibrium temperature of the planet from our best-fitting model is 1100 K, comparable to the equilibrium temperature (1400 K) derived by Palle et al. (2017). At such temperatures, the abundance of TiO and VO is expected to be very low from equilibrium chemistry calculations, and thus may not be detectable. The enhanced Rayleigh scattering observed in WASP-127b (Fig. 11) is qualitatively comparable to the results of Palle et al. (2017) and Chen et al. (2018). However, quantitatively the best-fitting model for Palle et al. (2017) has a Rayleigh enhancement factor of 5 while in Chen et al. (2018) this value is in the range of ∼ 8500–250 000. Quantitatively, the results differ due to differences in the adopted models and model choices. While Palle et al. (2017) used forward models with and without TiO/VO with a maximum Rayleigh scattering enhancement of five times the nominal Rayleigh scattering, Chen et al. (2018) used free retrievals with priors on the Rayleigh scattering enhancement factor ranging from 10^{-4} to 10^{10}. In this work, we compute a forward model grid with equilibrium chemistry and Rayleigh scattering enhancement factor going from 1 to 1100 times the multigas Rayleigh scattering.

The enhanced Rayleigh scattering slope has been observed for other planets like HD 189733b (Sing et al. 2011), WASP-94b (Ahrer et al. 2022), WASP-127b (Palle et al. 2017), WASP-21b (Alderson et al. 2020), etc. This can be due to an additional opacity source like a mineral cloud (Lecavelier Des Etangs et al. 2008) or a photochemical hazes (Kawashima & Ikoma 2019; Ohno & Kawashima 2020) or a combination of clouds and hazes (Pont et al. 2013). Unocculted starspots can also mimic the Rayleigh scattering slope (McCullough et al. 2014; Rackham et al. 2017). However, Spake et al. (2021) found that WASP-127 is a photometrically quiet star from the *TESS* light curves, thus implying that the stellar inhomogeneities are unlikely to be the case here.

Even though HFOSC observations of HAT-P-1b are in good agreement with Gemini/GMOS observations (Todorov et al. 2019) (Fig. 10), the Gemini/GMOS observations suffers from strong systematic effects leading to large uncertainties comparable to HCT/HFOSC. The observed equilibrium temperature from both HFOSC (1472 K) and Gemini/GMOS (1500 K) are also comparable to each other. We estimated the transmission spectrum metric (TSM) values from Kempton et al. (2018) for all three planets. The TSM values are proportional to the SNR expected from the transmission spectra considering the transit depth and the scale height excluding the potential impact of clouds. The TSM values for KELT-18b, WASP-127b, and HAT-P-1b are 77.30, 447.68, and 196.67, respectively. The lower TSM value of KELT-18b implies that the observed featureless spectra is a combination of poor SNR and the inherently small-scale height of the planet even though the clouds or hazes can mute the absorption features. The lower SNR can be due to a less suitable comparison star and a larger separation between the star and the reference star. The equilibrium temperature determined by McLeod et al. (2017) for KELT-18b is 2085 K, which is 885 K higher than the best-fitting equilibrium temperature from our study.

Considering a visual magnitude of less than 12 and planets orbiting around main sequence dwarf stars with TSM greater than 99 and a transit duration under 7 h, and most importantly, ensuring a reference star with a maximum separation of 11 arcmin, we expect to characterize 25 more exoplanet atmosphere from HCT/HFOSC. In a broader sense, this proof-of-concept study paves the way for examining the atmospheres of exoplanets using other relatively small telescopes that are outfitted with comparable spectrographic instruments. Our analysis combining HFOSC observations with infrared observations from *HST* or/and *Spitzer* proves that HFOSC can be an alternative optical instrument to use in conjunction with space-based infrared instruments like *HST*, *Spitzer*, and *JWST*.

DATA AVAILABILITY

Spectroscopic data of all three targets will be provided by the corresponding author upon reasonable request.

REFERENCES

Ahrer E., Wheatley P. J., Kirk J., Gandhi S., King G. W., Louden T., 2022, MNRAS, 510, 4857

Alderson L. et al., 2020, MNRAS, 497, 5182

Amundsen D. S., Baraffe I., Tremblin P., Manners J., Hayek W., Mayne N. J., Acreman D. M., 2014, A&A, 564, A59

Appenzeller I. et al., 1998, The Messenger, 94, 1

Astropy Collaboration 2013, A&A, 558, A33

Bean J. L., Miller-Ricci Kempton E., Homeier D., 2010, Nature, 468, 669

Bean J. L. et al., 2011, ApJ, 743, 92

Bonomo A. S. et al., 2017, A&A, 602, A107

Brown T. M., 2001, ApJ, 553, 1006

Carter A. L. et al., 2020, MNRAS, 494, 5449

Casasayas-Barris N. et al., 2022, A&A, 664, A121

Charbonneau D., Brown T. M., Noyes R. W., Gilliland R. L., 2002, ApJ, 568, 377

Chen G., Pallé E., Welbanks L., Prieto-Arranz J., 2018, A& A, 616, A145

Chen G., Casasayas-Barris N., Pallé E., Welbanks L., Madhusudhan N., Luque R., Murgas F., 2020, A&A, 642, A54

Chen G., Wang H., van Boekel R., Pallé E., 2022, AJ, 164, 173

Dressler A. et al., 2011, PASP, 123, 288

Drummond B., Tremblin P., Baraffe I., Amundsen D. S., Mayne N., Venot O., Goyal J., 2016, A&A, 594, A69

Foreman-Mackey D., Hogg D. W., Lang D., Goodman J., 2013, PASP, 125, 306

Gibson N. P., Aigrain S., Barstow J. K., Evans T. M., Fletcher L. N., Irwin P. G. J., 2013, MNRAS, 436, 2974

Giménez A., 2006, A&A, 450, 1231

Goyal J. M. et al., 2017, MNRAS, 474, 5158

Goyal J. M., Wakeford H. R., Mayne N. J., Lewis N. K., Drummond B., Sing D. K., 2018, MNRAS, 482, 4503

Goyal J. M. et al., 2020, MNRAS, 498, 4680

Hook I. M., Jørgensen I., Allington-Smith J. R., Davies R. L., Metcalfe N., Murowinski R. G., Crampton D., 2004, PASP, 116, 425

Hunter J. D., 2007, Comput. Sci. Eng., 9, 90

Jiang C., Chen G., Pallé E., Parviainen H., Murgas F., Ma Y., 2022, A&A, 664, A50

Jiang C., Chen G., Pallé E., Murgas F., Parviainen H., Ma Y., 2023, A&A, 675, A62

Jordán A. et al., 2013, ApJ, 778, 184

Kawashima Y., Ikoma M., 2019, ApJ, 884, 98

Kempton E. M. R. et al., 2018, PASP, 130, 114401

Lam K. W. F. et al., 2017, A&A, 599, A3

Lecavelier Des Etangs A., Vidal-Madjar A., Désert J. M., Sing D., 2008, A&A, 485, 865

Lendl M. et al., 2016, A&A, 587, A67

Mallonn M., Strassmeier K. G., 2016, A&A, 590, A100

Mandel K., Agol E., 2002, ApJ, 580, L171

Maxted P. F. L., Gill S., 2019, A&A, 622, A33

May E. M., Gardner T., Rauscher E., Monnier J. D., 2019, AJ, 159, 7

McCullough P. R., Crouzet N., Deming D., Madhusudhan N., 2014, ApJ, 791, 55

McLeod K. K. et al., 2017, AJ, 153, 263

Montalto M., Iro N., Santos N. C., Desidera S., Martins J. H. C., Figueira P., Alonso R., 2015, ApJ, 811, 55

Murgas F., Pallé E., Zapatero Osorio M. R., Nortmann L., Hoyer S., Cabrera-Lavers A., 2014, A&A, 563, A41

Murgas F., Chen G., Pallé E., Nortmann L., Nowak G., 2019, A&A, 622, A172

Nascimbeni V. et al., 2013, A&A, 549, A30

Nikolov N. et al., 2014a, MNRAS, 437, 46

Nikolov N. et al., 2014b, MNRAS, 447, 463

Nikolov N., Sing D. K., Gibson N. P., Fortney J. J., Evans T. M., Barstow J. K., Kataria T., Wilson P. A., 2016, ApJ, 832, 191

Nikolov N. et al., 2018, Nature, 557, 526

Nortmann L., Pallé E., Murgas F., Dreizler S., Iro N., Cabrera-Lavers A., 2016, A&A, 594, A65

Ohno K., Kawashima Y., 2020, AAS/Division for Planetary Sciences Meeting Abstracts, 213.01

Palle E. et al., 2017, A&A, 602, L15

Panwar V., Désert J.-M., Todorov K. O., Bean J. L., Stevenson K. B., Huitson C. M., Fortney J. J., Bergmann M., 2022, MNRAS, 510, 3236

Parviainen H., 2015, MNRAS, 450, 3233

Parviainen H., 2020, MNRAS, 499, 1633

Pont F., Sing D. K., Gibson N. P., Aigrain S., Henry G., Husnoo N., 2013, MNRAS, 432, 2917

Rackham B. et al., 2017, ApJ, 834, 151

Rackham B. V., Apai D., Giampapa M. S., 2018, ApJ, 853, 122

Sánchez-Janssen R., Mieske S., Selman F., Bristow P., Hammersley P., Hilker M., Rejkuba M., Wolff B., 2014, A&A, 566, A2

Seager S., Sasselov D. D., 1998, ApJ, 502, L157

Seager S., Sasselov D. D., 2000, ApJ, 537, 916

Sedaghati E. et al., 2016, A&A, 596, A47

Sing D. K. et al., 2011, MNRAS, 416, 1443

Sing D. K. et al., 2012, MNRAS, 426, 1663

Sing D. K. et al., 2014, MNRAS, 446, 2428

Sing D. K. et al., 2016, Nature, 529, 59

Skaf N. et al., 2020, AJ, 160, 109

Snellen I. A. G., Albrecht S., de Mooij E. J. W., Le Poole R. S., 2008, A&A, 487, 357

Snellen I. A. G., de Kok R. J., de Mooij E. J. W., Albrecht S., 2010, Nature, 465, 1049

Spake J. J. et al., 2021, MNRAS, 500, 4042

Spyratos P. et al., 2021, MNRAS, 506, 2853

Stevenson K. B., Bean J. L., Seifahrt A., Désert J.-M., Madhusudhan N., Bergmann M., Kreidberg L., Homeier D., 2014, AJ, 147, 161

Todorov K. O. et al., 2019, A&A, 631, A169

Tody D., Hanisch R., Brissenden R., Barnes J., 1993, in Hanisch R. J., Brissenden R. J. V., Barnes J., eds, ASP Conf. Ser. Vol. 52, Astronomical Data Analysis Software and Systems II. Astron. Soc. Pac., San Francisco, p. 173

Tremblin P., Amundsen D. S., Mourier P., Baraffe I., Chabrier G., Drummond B., Homeier D., Venot O., 2015, ApJ, 804, L17

Virtanen P. et al., 2020, Nat. Methods, 17, 261

Wakeford H. R. et al., 2013, MNRAS, 435, 3481

van der Walt S., Colbert S. C., Varoquaux G., 2011, Comput. Sci. Eng., 13, 22

Weaver I. C. et al., 2019, AJ, 159, 13

Weaver I. C. et al., 2021, AJ, 161, 278

Wilson P. A. et al., 2015, MNRAS, 450, 192

Wilson J. et al., 2020, MNRAS, 497, 5155

Wilson J., Gibson N. P., Lothringer J. D., Sing D. K., Mikal-Evans T., de Mooij E. J. W., Nikolov N., Watson C. A., 2021, MNRAS, 503, 4787

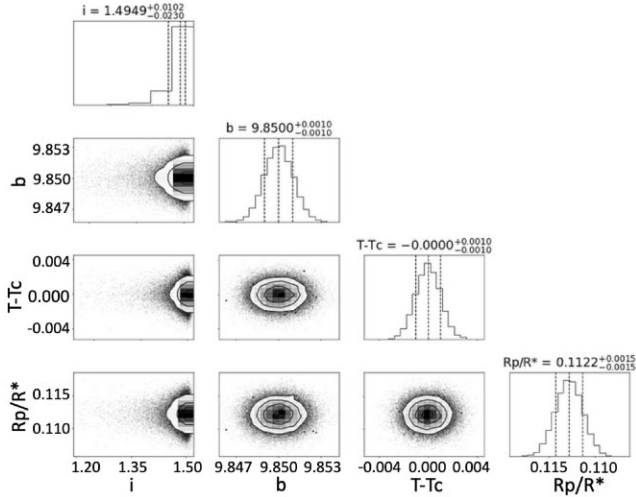Yan F. et al., 2020, A&A, 642, A98

APPENDIX A:

Figure A1. Posterior distribution of orbital inclination (i) in radians, impact parameter (b), the difference in mid-transit time $(T - T_c)$ with $T_C = 2459079.932$ (Nikolov et al. 2014a), and the planet to star radius ratio (R_p/R_*) from the best-fitting white light curve for HAT-P-1b.
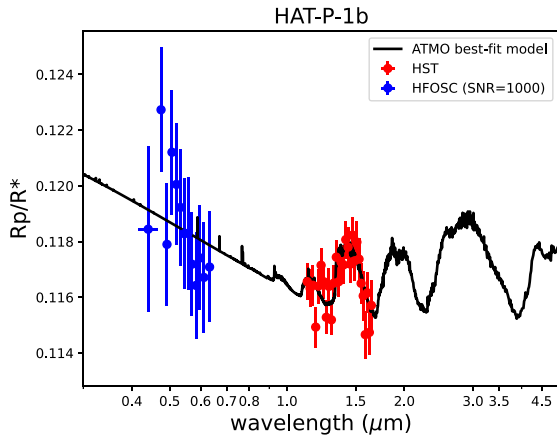

Figure A2. The best-fitting ATMO model for combined HFOSC (SNR = 1000) and infrared observations from *HST* (Wakeford et al. 2013) for the planet HAT-P-1b.
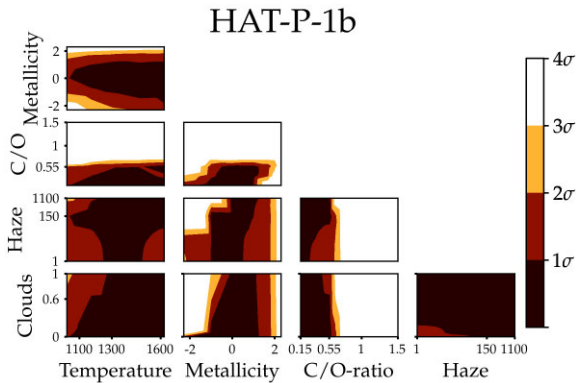

Figure A3. The χ^2 map for HAT-P-1b when fitting model grid to IR observations from *HST* Wakeford et al. (2013). The contour, colour maps, and labels are same as Fig. 12.
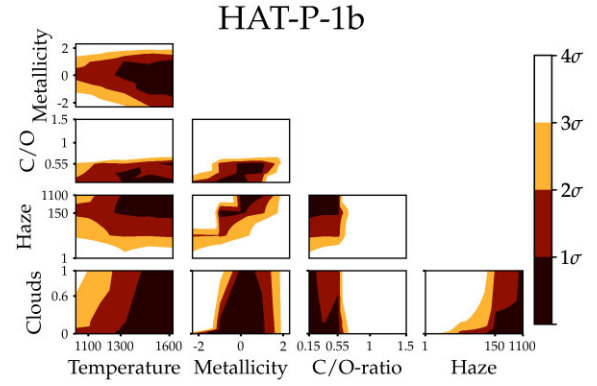
Figure A4. The χ^2 map for HAT-P-1b when fitting model grid to HFSOC observations from this work and IR observations from *HST* Wakeford et al. (2013). The contour, colour maps, and labels are same as Fig. 12.
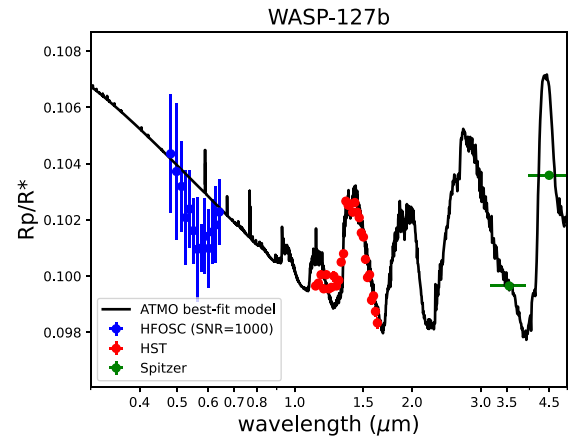

Figure A5. The best-fitting ATMO model for combined HFOSC (SNR = 1000) and *HST* in IR (Spake et al. 2021) for the planet WASP-127b.
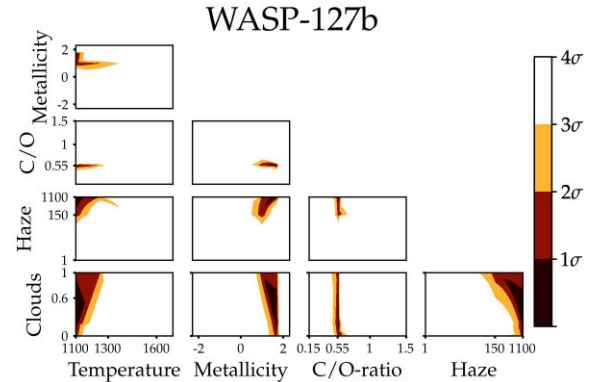

Figure A6. The χ^2 map for WASP-127b when fitting model grid to *HST* and *Spitzer* observations from Spake et al. (2021) in IR. The contour, colour maps, and labels are same as Fig. 12.
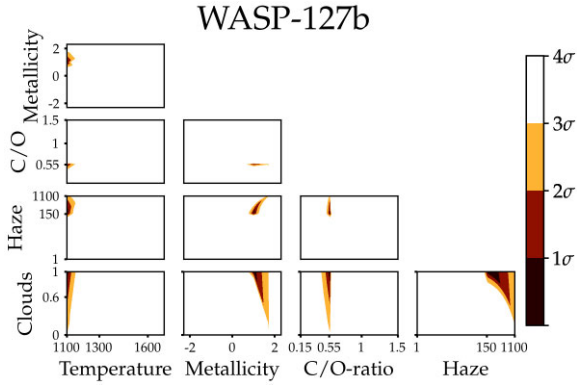
Figure A7. The χ^2 map for HAT-P-1b when fitting model grid to HFSOC observations from this work and *HST* plus *Spitzer* observations from Spake et al. (2021) in IR. The contour, colour maps and labels are same as Fig. 12.
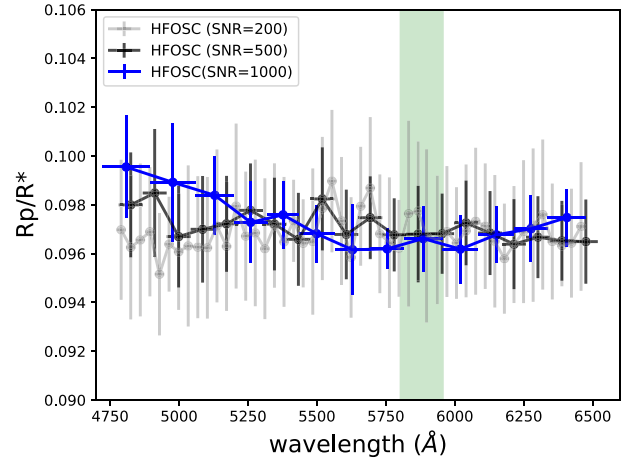

Figure A8. The observed transit spectra of WASP-127b in different wavelength bins SNR = 1000, SNR = 500, and SNR = 200. The vertical region in cyan shows the expected sodium doublet region. The Rayleigh scattering slope is not evident in both the transit spectra of SNR = 200 and SNR = 500.

This paper has been typeset from a T$_{\rm E}$X/L$^{\rm A}$T$_{\rm E}$X file prepared by the author.